Performance investigation of conduction-cooled cryogenic permanent magnet undulator at high beam currents

Jui-Che Huang,[1,*] Hideo Kitamura,[2] Chih-Shen Yang,[1] Ching-Kang Yang,[1] Chih-Wei Chen,[1] and Yu-Chun Chuang[1]

[1]National Synchrotron Radiation Research Center, Hsinchu Science Park, Hsinchu 30073, Taiwan
[2]Harima Institute, RIKEN, SPring8, 1-1-1 Kouto, Mikazuki-cho, Sayo-gun, Hyogo, 679-5148, Japan

(Received 30 October 2023; accepted 14 December 2023; published 6 February 2024)

A conduction-cooled cryogenic permanent magnet undulator, CU15, with a period length of 15 mm and 133 periods has been successfully developed. This undulator has been operated at the Taiwan Photon Source (TPS) storage ring at a beam current of 500 mA for more than 3 years. In CU15, two cryocoolers are used to cool the PrFeB magnets to 80 K. The effective magnetic field measures 1.33 Tesla for a magnet gap of 4.2 mm, maintaining an rms phase error below 2.6°. The bunch length of the electron beam in TPS is as short as 16 psec, leading to a serious issue with high beam-induced heating in CU15. This report addresses the above issues and provides detailed adaptations of CU15 to operate at a beam current of 500 mA.

DOI: 10.1103/PhysRevAccelBeams.27.023501

I. INTRODUCTION

In advanced synchrotron light sources, using short-period undulators with high magnetic fields and low phase errors can significantly enhance the spectral performance of synchrotron radiation sources. Short-period undulators can generate photons of shorter wavelengths at lower beam energies, maximizing the photon energy tuning range and enhancing user convenience. Cryogenic permanent magnet undulators (CPMUs) are specifically developed to fabricate undulators with short periods and small gaps, offering several advantages: (i) CPMUs integrate with the well-established in-vacuum undulators (IVUs) technologies, simplifying the initiation of short-period undulator development, (ii) At cryogenic temperatures (CT), the remanence and coercivity of magnets increase significantly, resulting in a 30% higher magnetic field compared to an IVU with the same magnet circuit design. The increased magnetic field allows for a reduction in the undulator period while maintaining a reasonable undulator K value. (iii) The substantial increase in coercivity enhances the magnet's resistance against radiation-induced demagnetization, enabling the use of a smaller magnet gap. (iv) CPMUs can achieve ultrahigh vacuum (UHV) conditions without any bake-out due to the suppression of outgassing from permanent magnets (PMs) at CT. Additionally, all cold surfaces of the PMs, along with the in-vacuum girders, function as cryopumps. As a result, nonbaked CPMUs can operate in a storage ring without any problem.

The small-gap CPMU in a storage ring presents several challenges, including beam lifetime, dynamic aperture for injection, radiation-induced demagnetization, beam-induced heating, and operational safety margins. Although many CPMUs operate in storage rings [1–5], there are limited reports addressing these challenging issues. In the critical topic of beam-induced heating, studies of superconducting undulators with cold vacuum chambers [5–8] have revealed that the measured beam-induced heating is higher than expected from synchrotron radiation (SR) from upstream bending magnets and resistive wall heating (image current heating). These researches suggest that the mechanism behind beam-induced heating is not yet fully understood. The storage ring of the TPS is currently operating at a beam current of 500 mA with a short bunch length (∼16 ps), leading to significant challenges related to the high beam-induced heating deposited on each component in CPMUs.

This paper presents an overview of the CPMU (CU15) installed at the Taiwan Photon Source (TPS) and addresses the challenges related to beam-induced heating that occurred during its operation. The technical sections begin from Secs. II to IV. Section II highlights the uniquely key features and design concepts of CU15, while Sec. III demonstrates its magnetic and cryogenic performance. In Sec. IV, the beam-induced heating mechanism is investigated when CU15 operates at a beam current of 500 mA in the TPS storage ring. Finally, the vibration issue derived from the cryocoolers is presented.

*Corresponding author: huang.juiche@nsrrc.org.tw

TABLE I. Main parameters in various operating modes of CU15.

Items	Unit	Room temperature	Cryogenic temperature		
			Mode A	Mode B	Mode C[c]
Beam current, I_{beam}	mA	⋯	500	400	500
Magnet temperature, T_{mag}	K	300	80	80	80
Magnet material			$Pr_2Fe_{14}B$ (NMX-68CU)		
Remanence, B_r	T	1.41	1.64		
Coercivity, H_{cj}	kA/m	1740	6385		
Period length, λ_u	mm	15.00	14.95		
Number of periods, N_u			133		
Minimum magnet gap, $(G_{\mathrm{mag}})_{\mathrm{min}}$[a]	mm	4.2	5.2	4.2	20
Maximum effective magnetic field, $(B_{\mathrm{eff}})_{\mathrm{max}}$	T	1.17	1.02	1.33	0.04
Maximum deflection parameter, K_{max}[b]		1.64	1.42	1.85	0.06
Maximum attractive force, F_{max}	kN	25.8	19.4	33.5	0.03

[a]Minimum vacuum gap (beam stay clear), $(G_{\mathrm{vac}})_{\mathrm{min}}$, is 0.2 mm smaller than $(G_{\mathrm{mag}})_{\mathrm{min}}$.
[b]$K = 0.934\, B_{\mathrm{eff}}(\mathrm{T})\, \lambda_u(\mathrm{cm})$.
[c]Commissioning.

II. SPECIFICATION OF TPS-CPMU, CU15

The TPS-CPMU, CU15, is designed to have a minimum magnet gap, G_{mag} of 4.2 mm to achieve a maximum magnetic field of 1.33 Tesla. The permanent magnet array is covered with a double layer of copper (0.05 mm) and nickel (0.05 mm) metal sheet to prevent the generation of wake fields from the magnets, resulting in a minimum vacuum gap, G_{vac} of 4.0 mm. The technical specifications of CU15 are detailed in Table I, and a photograph of CU15 installed at the TPS storage ring is provided in Fig. 1. At CT, there are three operating modes: mode A is the standard operational mode with a 5.2 mm magnet gap and 500 mA beam current; mode B is reserved for operation with a 4.2 mm magnet gap and 400 mA beam current; and mode C was used with a 20 mm magnet gap during the commissioning phase.

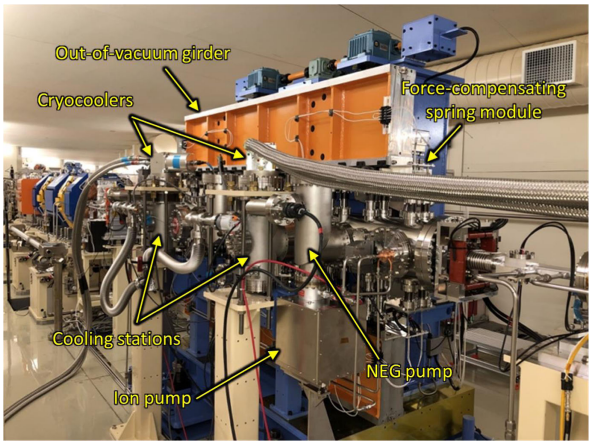

FIG. 1. TPS-CPMU, CU15 installed in the TPS storage ring.

A. Various components for CU15

The CU15 integrates several advanced techniques, allowing it to operate at high beam currents while maintaining high magnetic performance. Most CPMUs developed to date use liquid nitrogen circulating directly into a through hole within the in-vacuum girder [1–4]. In such a design, the welded parts of the liquid nitrogen channels are located within the ultrahigh vacuum, which is connected to the accelerator vacuum. However, this approach is prohibited by TPS vacuum regulations because it poses a significant risk to the accelerator vacuum. To address this issue, the cooling system of the CU15 employs conduction cooling with two cryocoolers. Figure 2 illustrates the magnet arrays, the vacuum system (consisting of two ion pumps with a pumping speed of 128 L/sec and five nonevaporable getter (NEG) pumps with a pumping speed of 500 L/sec), and two sets of low-vibration Gifford-McMahon cryocoolers (Leybold 250MD).

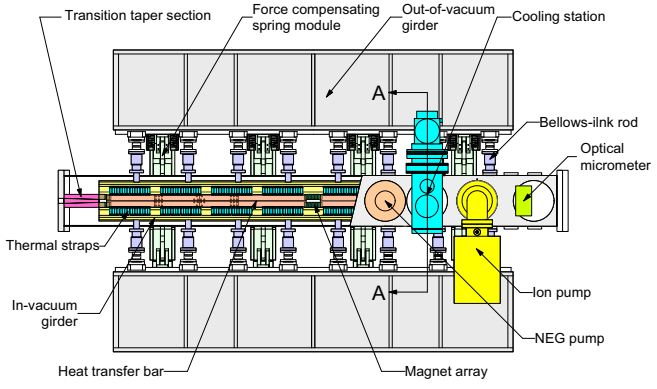

FIG. 2. Sketch of CU15; an A-A arrow view is shown in Fig. 3.

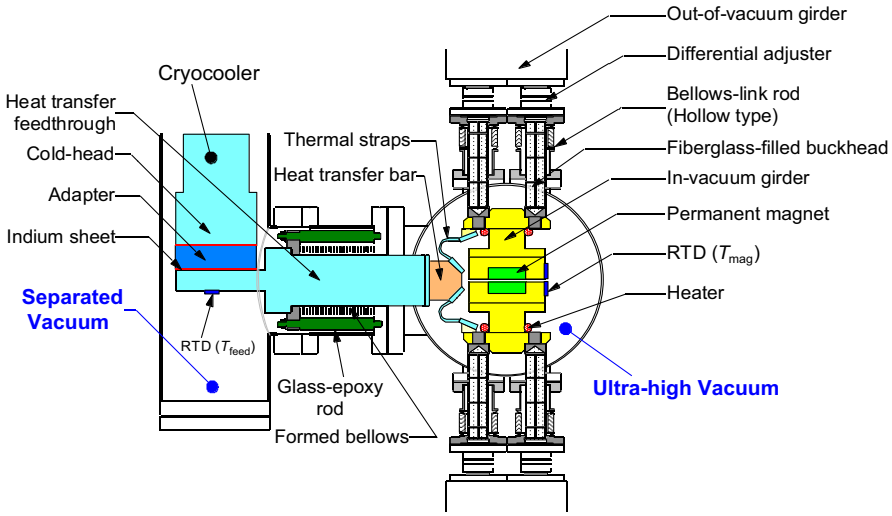

FIG. 3. A-A arrow view in Fig. 2. RTD denotes resistance temperature detector.

Figure 3 shows a detailed view of the cooling system. The cold head, a component of the cryocooler, is located in a separate vacuum chamber and is connected to the magnet array via flexible thermal straps and heat transfer feedthrough. These feedthroughs are not only responsible for conduction cooling but also divide the vacuum into UHV and separated vacuum sections. As a result, this design ensures that the vacuum system in the storage ring does not need to be evacuated during cryocooler maintenance. The conduction cooling design offers versatility in cooling methods, accommodating either cryocooler or liquid nitrogen (LN_2) tank cooling, depending on the specific application [9].

The following discussions present several key features of CU15:

1. Permanent magnet array

Magnets made from NdFeB and PrFeB materials are commonly used in CPMUs. PrFeB magnets are the preferred choice because of their ability to maintain a monotonic increase in both remanent field and coercive force at low temperatures. The use of NdFeB magnet is limited to $140 \sim 150$ K due to spin reorientation. To ensure a high remanent field at CT, and moderate coercive force at room temperature, a new grade of PrFeB permanent magnet material (NMX-68CU) has been developed, with a remanent field of 1.67 Tesla at 80 K and a coercive force of 1680 kA/m at 300 K [10]. This material can provide a high magnetic field at cryogenic temperature while avoiding demagnetization during assembly at room temperature.

2. In-vacuum girder

The magnet arrays, which consist of permanent magnets mounted on in-vacuum girders, are illustrated in Fig. 2. Compared to aluminum in-vacuum girders, oxygen-free high conductivity (OFHC) copper girders demonstrate significantly superior thermal conductivity, exceeding 2.5 times that of aluminum at 80 K, and their rigidity is nearly double that of aluminum girders. Moreover, the thermal shrinkage of OFHC copper girders is about 80% that of aluminum girders. Consequently, OFHC copper is a more preferable material choice for in-vacuum girders, ensuring low phase error characteristics.

3. Hollow type bellows-link rods

The upper and lower in-vacuum girders at 80 K are connected to the out-of-vacuum girders at 300 K using bellows-link rods. These rods are designed to have thin walls and hollow inner sections to minimize the conduction of heat transfer. The air circulation inside the hollow section of the link rods may cause condensation and additional convection heat transfer. To avoid this, laminated fiberglass separated by aluminum foil is inserted into the hollow section. The optimal number of bellows-link rods must be carefully determined to balance the tradeoff between low heat transfer and low phase errors, which arise from the deformation of the in-vacuum girders. In the CU15, a total of 32 link rods have been employed along the upper and lower in-vacuum girders.

4. Heat transfer feedthrough, heat transfer bar, and thermal straps

The conduction cooling mechanism is utilized in CU15, as illustrated in Fig. 3. The conduction cooling system comprises heat transfer feedthroughs, heat transfer bars, and several thermal straps. A total of 40 thermal straps are linked between the in-vacuum girders and the heat transfer bars to achieve good heat transfer characteristics and ensure temperature uniformity across the magnet arrays. These thermal straps primarily consist of flexible OFHC copper

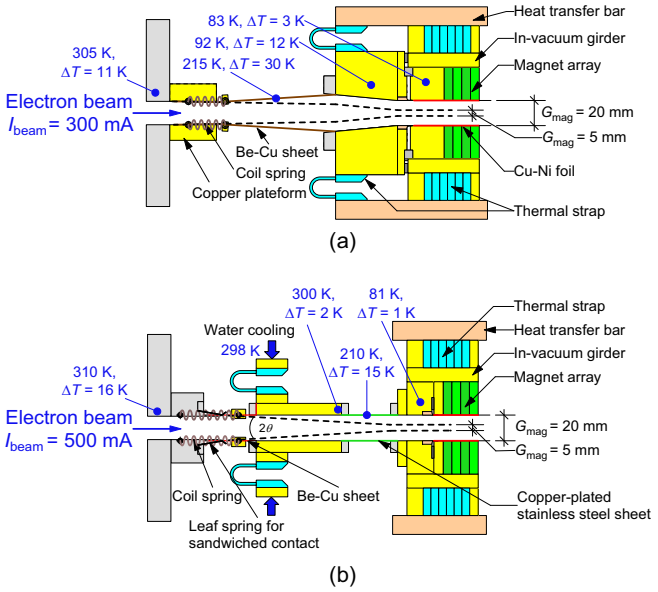

FIG. 4. Two types of transition tapers used in CU15, (a) prototype and (b) improved type with water cooling channel. The temperatures under operational conditions and the temperature increase from the no-beam condition are presented.

ropes that can allow any gap variations and thermal expansion or contraction that may occur between the in-vacuum girders and the heat transfer bars. The heat transfer feedthrough, consisting of (i) an OFHC copper cylinder brazed to a flange and supported by multiple glass-epoxy rods and (ii) formed bellows attached to the feedthrough are utilized not only to isolate the ultrahigh vacuum of the storage ring from the lower vacuum of the cold head but also to minimize conduction heat transfer from the vacuum chamber at room temperature to the heat transfer feedthrough at CT. The heat transfer bars are assembled alongside the magnet arrays, functioning not only as components of the conduction cooling system but also as thermal shields for the magnets during high-temperature activation of the NEG pumps.

5. Transition tapers

The transition tapers are positioned at both ends of CU15. They need to have a certain displacement allowance to accomodate the gap variations and the longitudinal thermal expansion/contraction of the magnet arrays. For CPMUs, in addition to these requirements, a low thermal conductivity is necessary for the transition taper to intercept the heat flow from the vacuum chamber to the magnet arrays. Figure 4(a) illustrates a prototype of the transition taper. A 0.2 mm thick Be-Cu sheet is affixed to one end of the magnet arrays while the other end can slide on the copper platform using coil springs. During the commissioning stage as shown in mode C in Table I, it was observed that the magnet temperature could not be maintained at the specified temperature of 80 K when the beam current exceeded 300 mA. This problem may be attributed to the cavities formed in the transition taper at wide gaps. Besides, the high deformability of long and thin beryllium copper (BeCu) sheets, designed to simplify the manufacturing process, can create similar cavitylike structures at smaller gaps. When the electron beam passes through cavitylike taper section, it loses some of its energy due to the geometric impedance. Part of the energy loss appears as microwaves either trapped in the taper section or propagate along the orbit and generate heat in the tapers or the magnet arrays. Furthermore, external microwaves are also propagating and trapped within the cavitylike structure, causing an increase in the temperature of the transition tapers. In other words, all the heat generated at the tapers becomes a load on the cryocoolers.

To solve the above problem, an improved transition taper with a water-cooled section in the middle has been adopted as shown in Fig. 4(b). This improved type aims to mitigate microwaves resulting from beam energy loss in the straight tapered structure, consequently minimizing heat generation from trapped microwaves. The taper angle, denoted as θ, is intentionally designed to remain small at varying magnetic gap values to prevent the formation of any cavity structure. The variation of θ ranges from $-0.7°$ (for $G_{\mathrm{mag}} = 25$ mm) to 4.0° (for $G_{\mathrm{mag}} = 5$ mm). Water cooling can efficiently absorb the majority of the heat generated in the taper section, thereby reducing the load on the cryocoolers. A double-layer sheet of 0.15 mm thick stainless steel sheet plated with 0.01 mm thick copper is used at the connection to the magnet array to obtain not only low image current heating but also high thermal insulation characteristics for the magnet array. It is noteworthy that the implementation of this improved type has facilitated the stable operation of CU15, even at a beam current of 500 mA, as will be explained later.

6. Temperature control system

A temperature control system is installed for both the upper and lower in-vacuum girders, to which the magnets are attached. Each girder is equipped with 2 sets of heaters and 14 temperature sensors, including 2 reference sensors. These sensors and heaters are divided into two temperature control loops, enabling independent control of the front and rear sections of the girder. Its primary purpose is to maintain a constant temperature for the magnets, regardless of operational storage ring modes or undulator gap conditions. Therefore, CU15 can generate reproducible energy spectra, due to the constant temperature of magnets. Since the spread of the synchrotron radiation emitted by an upstream bending magnet varies along the longitudinal beam path. The uneven thermal distribution can cause increased phase errors during the operation of the storage ring. To address this issue, the system allows for the adjustment of individual heaters to eliminate the

temperature gradient generated in the magnet arrays. This adjustment minimizes field errors arising from thermal effects such as (i) gap errors caused by temperature-dependent material deformations and (ii) variations in remanent fields along the PM magnet arrays. Additionally, this temperature control system can be utilized as a method for measuring beam-induced heating, as discussed later in this paper.

III. CRYOGENIC AND MAGNETIC PERFORMANCE

A. Cryogenic performance

1. Performance of cooling source

The cooling capacity of cryocoolers, associated with the temperature of the cold head, can be estimated using the cooling map provided by the vendor. However, this method cannot be used with the current system because it is difficult to access the cold-head temperature directly. Therefore, a separate test system where an additional heater was set up to measure the cooler's capacity as a function of the temperature, T_{feed}, of the feedthrough. The sensor for measuring T_{feed}, is attached to the end of the feedthrough as shown in Fig. 3. Consequently, the dependence of the cooling capacity of a single cryocooler on the feedthrough temperature, T_{feed}, is obtained as shown in Fig. 5.

2. System heat load and cooling margin

When CU15 operates with the magnet temperature controlled at a certain temperature, T_{mag}, in the absence of the electron beam condition, the following equation holds at the state of equilibrium:

$$P_{\mathrm{cooler}}(T_{\mathrm{feed}}) = P_{\mathrm{cond}}(T_{\mathrm{mag}}) + P_{\mathrm{rad}}(T_{\mathrm{mag}}, G_{\mathrm{mag}}) + P_{\mathrm{heater},0}, \tag{1}$$

where P_{cooler} represents the cooling capacity of the two cryocoolers; P_{cond} denotes the thermal conduction input power; P_{rad} indicates the thermal radiation power, and $P_{\mathrm{heater},0}$ stands for the output power of the heaters at beam current equals zero.

When the beam current is zero, the power of the heater, $P_{\mathrm{heater},0}$, can be defined as a measure of cooling margin, P_{margin}. The term "cooling margin" is defined to determine the amount of available power that can compensate for the dissipated power from the electron beam. Another definition is the system heat load, P_{system}, defined as the sum of thermal conduction power and thermal radiation power. Namely,

$$P_{\mathrm{system}}(T_{\mathrm{mag}}, G_{\mathrm{mag}}) = P_{\mathrm{cond}}(T_{\mathrm{mag}}) + P_{\mathrm{rad}}(T_{\mathrm{mag}}, G_{\mathrm{mag}}). \tag{2}$$

Accordingly, Eq. (1) can be rewritten as follows:

$$P_{\mathrm{cooler}}(T_{\mathrm{feed}}) = P_{\mathrm{system}}(T_{\mathrm{mag}}, G_{\mathrm{mag}}) + P_{\mathrm{margin}}(T_{\mathrm{mag}}, G_{\mathrm{mag}}). \tag{3}$$

The cooling margin can be measured at various temperatures of magnet at each magnet gap as illustrated in Fig. 6. At 80 K, the cooling margin is approximately 90 W. Therefore, the cooling efficiency, calculated as the available cooling on magnets divided by the cooling capacity from the cryocooler, from the conduction cooling system in the CU15 is about 40%. A smaller gap and higher magnet temperature lead to a larger cooling margin. The reason for

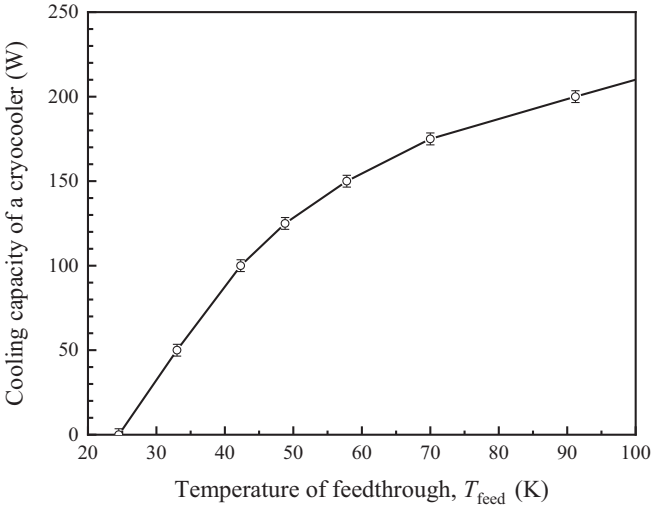

FIG. 5. Dependence of cooling capacity of a single cryocooler (Leybold 250MD) on the temperature of the feedthrough, T_{feed}.

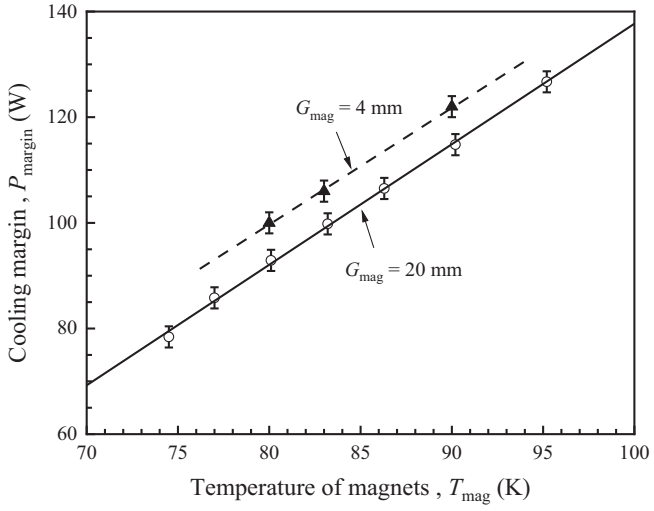

FIG. 6. Dependence of the cooling margin on the temperature of magnets.

TABLE II. Calculated system heat load, P_{system}, at $T_{mag} = 80$ K and $G_{mag} = 20$ mm.

Sources		Power (W)
Thermal conduction	Bellows-link rods (32 pcs)	72
	Transition tapers (4 pcs)	12
Thermal radiation from the vacuum chamber[a]		72
P_{system} (total)		156

[a]The emissivity of the in-vacuum girder made of OFHC is assumed to be 0.09.

this is that a smaller gap reduces the effective irradiation area for thermal radiation from the upper and lower in-vacuum girders. Consequently, a smaller P_{system} results in a larger cooling margin.

As shown in Fig. 7, the system heat load, which varies with magnet temperature, can also be determined using Eq. (3). The terms "cooling capacity of the cryocooler" and "cooling margin" in Eq. (3) can be referenced in Figs. 5 and 6, respectively. During the initial design stage, the system heat load was evaluated using "SOLIDWORKS," and the results are presented in Table II. The calculated value of P_{system} at $T_{mag} = 80$ K is 156 W, which aligns well with the measured value as shown in Fig. 7.

3. Lowest temperature and temperature stability

The vacuum pressure and magnet temperature over time, throughout the cooling process, are shown in Fig. 8. The magnet temperature reaches 80 K after 30 h, eventually stabilizing at a minimum temperature of 55 K. Simultaneously, the final vacuum pressure in the unbaked vacuum chamber reaches 10^{-8} Pa.

Figure 9 shows the temperature variations along the magnet arrays, demonstrating the efficacy of the temperature control system in maintaining consistent magnet temperatures. The temperature fluctuations along the magnet arrays remain within the narrow range of ± 0.4 K, and the temperature gradient along the magnet arrays approaches zero, thereby minimizing phase errors.

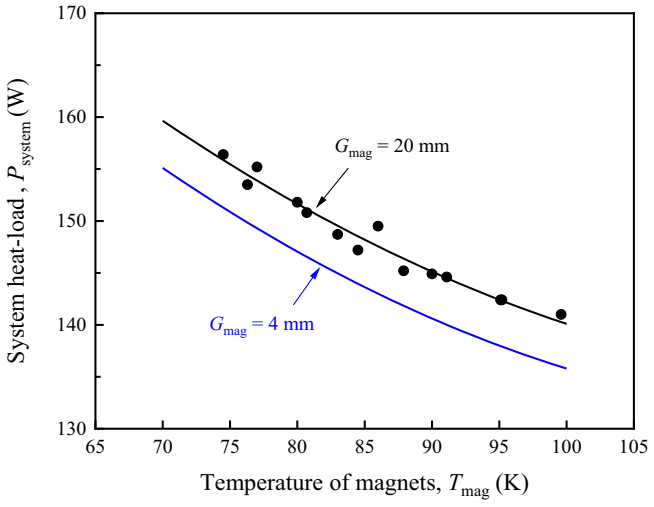

FIG. 7. Dependence of the system heat load on the temperature of the magnets.

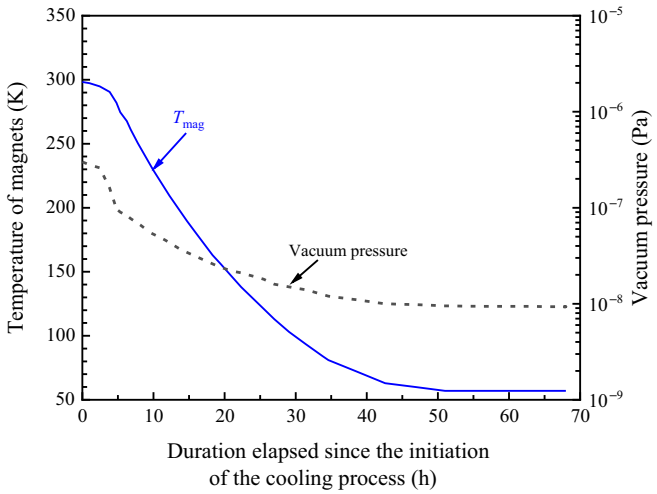

FIG. 8. Temperature of magnets and vacuum pressure changing over time during the cooling process.

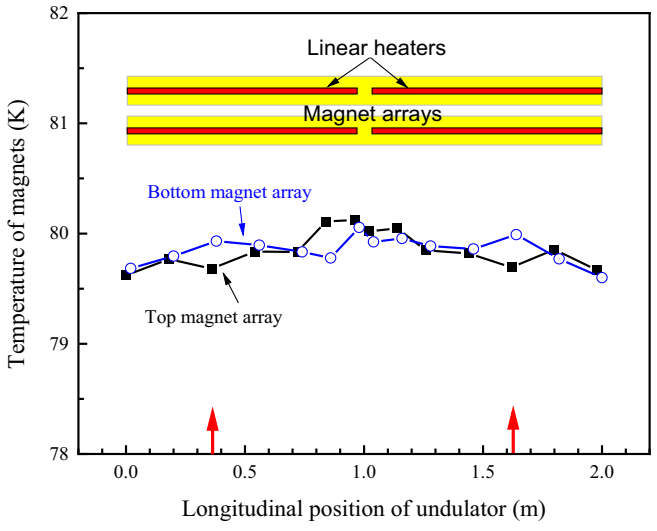

FIG. 9. Temperature distribution across the magnet arrays with a temperature-control system at $G_{mag} = 20$ mm. The two arrows on the horizontal axis indicate positions of the reference sensor.

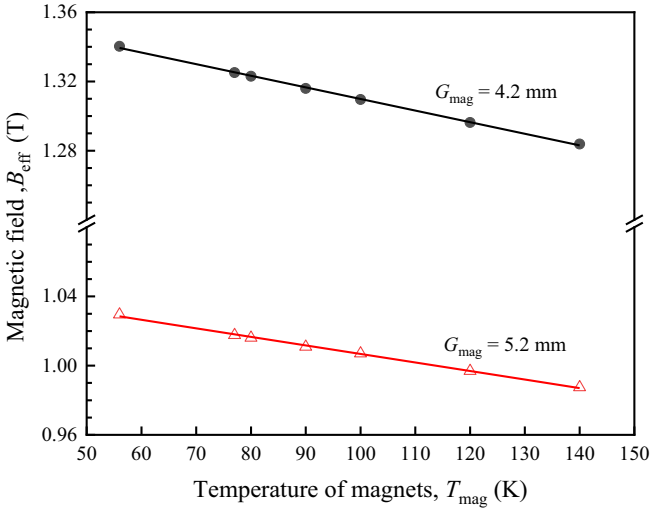

FIG. 10. Effective magnetic field varies with temperature of magnets.

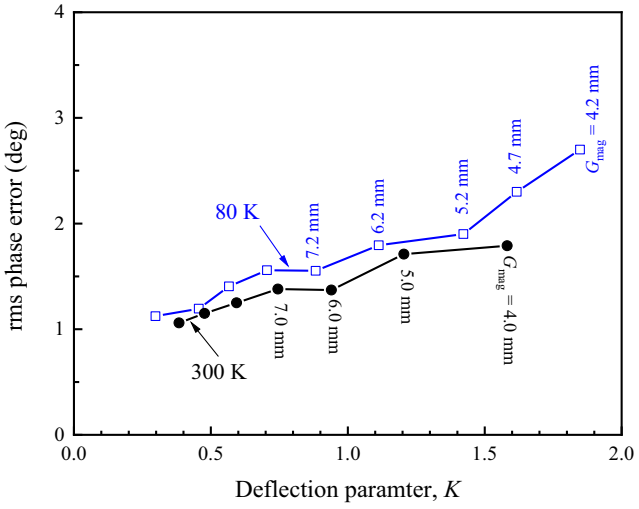

FIG. 11. rms phase error of CU15 varies with deflection parameter, K.

When operating under stable conditions, where magnet temperatures and the magnet gap remain constant, temperature fluctuations remain stable at ±0.1 K over several weeks. This stability enables precise control of the gap value within ±0.5 μm.

B. Magnetic performance

The CPMU project at TPS encompasses not only an undulator but also an *in situ* measurement system of the in-vacuum type [11] and temperature-dependent hall probe calibration [12] to precisely measure magnetic performances and give several field corrections when the CPMU is in CT mode. After cooling the magnets, the actual magnet gaps are wider than the gap value derived from the encoder value that measures the distance between the upper and lower out-of-vacuum girders. Therefore, the magnet gap is directly measured using two optical micrometers positioned at each end of the magnet array. Figure 10 shows the relationship between magnet temperature and the effective magnetic field. The effective magnetic field is important for spectral analysis, the effective magnetic field can be defined as $B_{\mathrm{eff}} = \sqrt{\sum_n^{\infty} B_n^2/n^2}$ [13], where B_n is the magnetic field harmonic components from a discrete Fourier transform. As the temperature decreases from 140 to 55 K, the effective magnetic field exhibits a linear increase both at the magnetic gap of 4.2 and 5.2 mm. Specifically, at a temperature of $T_{\mathrm{mag}} = 80$ K, the effective magnetic field is 1.33 and 1.02 Tesla at G_{mag} of 4.2 and 5.2 mm, respectively. Due to the magnetic properties, there is a 16% increase in the remanence field from 300 to 80 K. Therefore, the observed approximately 14% increase in the magnetic field compared to that at room temperature aligns with expectations. An advanced undulator requires low rms phase error characteristics. Phase errors can be effectively minimized through well-established field correction methods at room temperature. However, when a CPMU operates at CT, phase errors can increase due to the higher K value, even in the absence of additional field errors. This increase occurs because phase error scales with $K^2/(1+K^2/2)$ [10]. Additionally, phase errors can substantially rise due to additional field errors originating from two sources: (i) static errors, which are independent of gaps and result from uneven material contractions within the bellows-link rods and in-vacuum girders, and (ii) dynamic errors, which are gap dependent and result from increased magnetic forces at CT. The former static field error can be corrected using differential adjusters. On the other hand, the latter dynamic error can be corrected by the force compensation spring modules [14]. These modules provide additional supporting points to minimize the deformation of out-of-vacuum girders and consequently reduce intrinsic phase errors. Moreover, a set of springs with different coefficients can create a multilinear approximation of the counterforce that compensates for the magnetic force, which varies exponentially with the gap value. These spring modules can be set up in-air to facilitate spring tuning, while CU15 operates in both RT and CT. Figure 11 illustrates the phase errors of CU15 are slightly increased at 80 K, and the rms phase errors are less than 2.6° for all gaps.

IV. BEAM-INDUCED HEATING

The high beam-induced heating may lead to the temperature gradient across the magnet arrays, potentially causing gap tapers or errors that could degrade the undulator's magnetic performance. To achieve a practical CPMU with low phase error, it is crucial to ensure sufficient cooling capacity to dissipate the beam-induced heat load and implement precise temperature control to remove the temperature gradient of magnets.

A. Calculated beam-induced heating

The beam-induced heating in CU15 can be derived from several known sources: (i) synchrotron radiation emitted from upstream bending magnets, (ii) resistive wall heating in the magnet arrays, (iii) internal microwave power associated with beam power loss attributed to the geometric impedance of the transition tapers and magnet arrays in CU15, (iv) external microwave power associated with beam power loss attributed to the geometric impedance of various components distributed throughout the storage ring, excluding CU15, and (v) indirect SR derived from simple reflection, fluorescence, or Compton scattering. Quantitatively evaluating the heat load of indirect SR is difficult. Therefore, indirect SR is not discussed in this paper.

The dissipated power from the electron beam, P_{beam}, given to the magnet arrays in a CPMU can be described by

$$P_{\mathrm{beam}} \approx P_{\mathrm{SR}} + P_{\mathrm{rw}} + P_{\mathrm{mw}}. \tag{4}$$

The first term, P_{SR}, in Eq. (4) is derived from the synchrotron radiation that is emitted from an upstream bending magnet. The power derived from the SR can be evaluated by the vertical distribution of the angular power density, as explained in Ref. [15]. The second term, P_{rw}, represents the power of resistive wall heating, uniformly distributed in the longitudinal direction, and can be calculated using an analytical formula provided in Ref. [16]. The third term, P_{mw}, represents microwave power, results from part of the beam energy loss, absorbed by the magnet arrays. The beam power loss in CU15, $P_{\mathrm{loss,CU15}}$, includes the magnet arrays and taper sections, so it can be estimated in

$$P_{\mathrm{loss,CU15}} = \Delta E / T_{\mathrm{b}}, \tag{5}$$

where,

$$\Delta E = k_{\mathrm{loss}} (I_{\mathrm{beam}} / N_b f_{\mathrm{rev}})^2, \tag{6}$$

and T_b is the bunch interval. I_{beam} denotes the beam current, N_b denotes the number of bunches, and f_{rev} is revolution frequency. The longitudinal loss factor, k_{loss}, can be evaluated using a 3D electromagnetic code (GdfidL [17]). Assuming that all beam power loss generated in CU15 becomes microwave power and absorbed by the magnet arrays, P_{mw} is equal to $P_{\mathrm{loss,CU15}}$. In this case, the calculated beam-induced heat load of CU15 from various sources is shown in Fig. 12. The parameters used in the calculation are shown in Table III. These beam parameters correspond to the TPS routine operations.

B. Measured beam-induced heat load

The cooling margin can remain constant through the precise temperature control on magnets, so the dissipated power by the electron beam can be tracked by monitoring the change in heater power as demonstrated in

$$P_{\mathrm{beam}} = P_{\mathrm{margin}} - P_{\mathrm{heater}}, \tag{7}$$

In the subsequent discussion, the estimation of power from the electron beam is using this method with a repeatability of approximately ± 1.5 W.

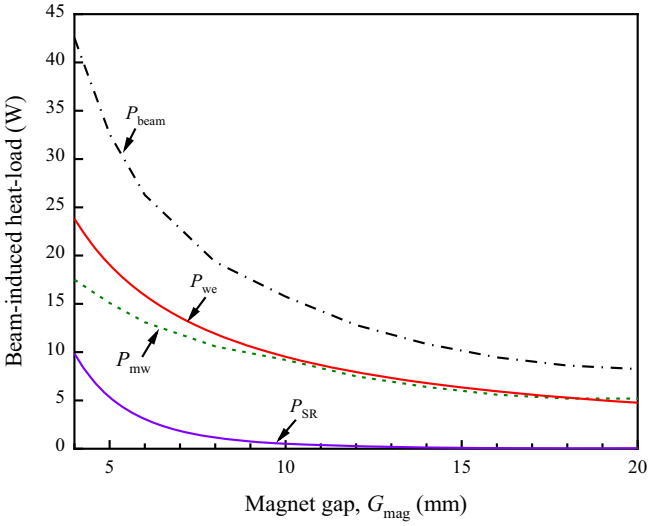

FIG. 12. Dependence of various beam-induced heat loads on the magnet gap in CU15 under the assumption that P_{mw} is equal to $P_{\mathrm{loss,CU15}}$. The calculation is based on the TPS parameters in Table III. The distance from the end of the upstream dipole magnet to the undulator entrance is 6 m. The results do not account for microwave power propagating from outside CU15. The calculation is based on $T_{\mathrm{mag}} = 80$ K and the bunch length of the electron beam is 16 ps.

1. Effect of the beam current on beam-induced heating

The initial measurement of beam-induced heat load was conducted at a wide gap of 20 mm, where expected a low heat-load result from SR emitted by an upstream bending

TABLE III. Beam parameters at TPS for routine operation.

Beam parameter		Value
Beam energy (GeV)	E_{GeV}	3.01
Beam current (mA)	I_{beam}	500
Emittance (nm·rad)	ε_x	1.6
Energy spread	σ_γ/γ	1.0×10^{-3}
Number of bunches	N_b	600 + 1 (single bunch)
rf harmonic number	H_{rf}	864
rf frequency (MHz)	f_{rf}	500
Bunch current (mA)		0.83 + 3.5 (single bunch)
Bunch interval (ns)	T_b	2
Revolution frequency (MHz)	f_{rev}	0.57

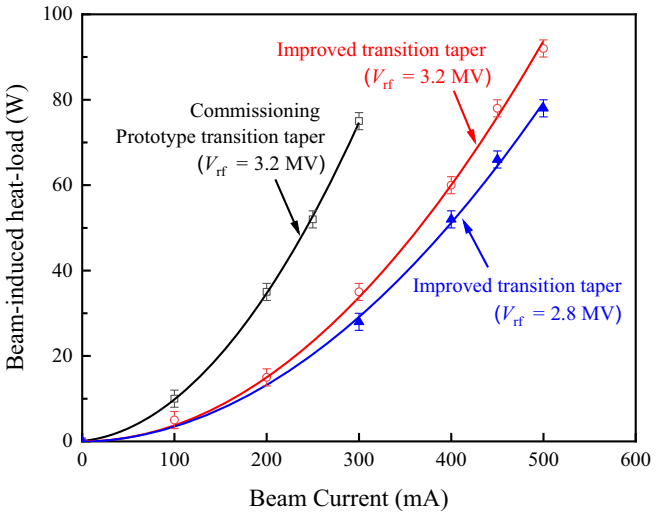

FIG. 13. Beam-induced heat load varies with beam current with $G_{mag} = 20$ mm and $T_{mag} = 80$ K. The solid lines represent quadratic curve fitting.

magnet and resistive wall heating. Figure 13 shows the measured beam-induced heat load varies with the beam current using different transition tapers. The measurement was conducted under a fixed condition, with $G_{mag} = 20$ mm and $T_{mag} = 80$ K, ensuring a constant cooling margin. The beam power loss in the prototype transition tapers shown in Fig. 4(a) is roughly twice as high as in the improved transition tapers shown in Fig. 4(b), which means that the microwave power to heat the magnet arrays is doubled. As a result, the cooling capacity becomes insufficient when the beam current exceeds 300 mA. However, after removing the cavitylike structure from the prototype transition tapers, the beam-induced heat load on the CU15 is significantly reduced to below 100 W at 500 mA. The measured data for beam-induced heat load showed a strong correlation with a quadratic dependence, indicating that the heating source is attributed to broadband impedance. If SR were the dominant heating source, one would expect a linear relationship between beam-induced heat load and beam current. A further point to note is that lowering the rf voltage can effectively reduce the heat load attributed to broadband impedance. This topic will be discussed in the following section.

2. Effect of bunch length on the beam-induced heating

The beam-induced heating is expected to be associated primarily with broadband impedance based on previous discussions. Therefore, the investigation of heat load in different rms bunch lengths has been conducted to identify this aspect. The rms bunch length was measured using a streak camera (Hamamatsu C10910) in various rf voltages and beam currents. Table IV shows that the bunch length increases with an increase in beam current or a decrease in rf voltage. The measurement of the bunch length has an error margin of 10%.

TABLE IV. Bunch length measured at various rf voltages and beam currents.

rf voltage (MV)	σ_t@$I_{beam} = 500$ mA (ps)	σ_t@$I_{beam} = 400$ mA (ps)
3.6	14	13
3.2	16	15
3.0	17	15.5
2.8	18	16.5
2.6	19	18

In Fig. 14, the measured values of P_{beam}/I_{beam}^2 are plotted against different bunch lengths. The results indicate that the beam-induced heat load decreases as the bunch length increases. The microwave power caused by geometric impedance and the power of resistive wall heating have different correlations between the bunch length and power, so the former can be expressed as $P_{mw} \propto {\sigma_t}^{-1}$ while the latter is given by $P_{rw} \propto {\sigma_t}^{-1.5}$ [8]. When the magnet gap is set at 20 mm, the curve shows a better fit between P_{beam}/I_{beam}^2 and ${\sigma_t}^{-1.1}$, suggesting that geometric impedance is dominant in the beam-induced heating. Conversely, when the gap is reduced to 5.2 mm, the curve is a better fit between P_{beam}/I_{beam}^2 and ${\sigma_t}^{-1.3}$, indicating that the resistive wall effect becomes more dominant at smaller gaps.

3. Temperature distribution of magnet arrays

The temperature distribution across the magnet arrays is examined at a beam current of 500 mA. The temperature deviation from the reference point (set at 80 K) is shown in Fig. 15. The temperature distribution profile is symmetrical and parabolic at the center of the magnet array, with temperature rises of the magnet array observed near both ends, which suggests that the contribution of SR irradiation is very small. Therefore, the temperature increase near both ends seems to be primarily due to microwaves propagating into the magnet gap from both ends of the magnet array. The temperature increases near both ends become more pronounced when the magnet gap is narrower and the bunch lengths are shorter. The phenomenon above can be explained by the microwaves passing through the magnet gap and being absorbed by the magnet array. A wider magnet gap may allow for a longer distance of microwave propagation, whereas a narrow gap may result in a shorter propagation distance. Consequently, when the magnet gap is narrow, temperatures near the ends of the magnet arrays are thought to be higher compared to the center.

At a magnet gap of 5.2 mm, a maximum temperature variation of ± 1.1 K was observed for a bunch length of 16 ps. Consequently, the increased temperature of magnets may lead to relative magnetic field errors and additional phase errors. The magnetic field of an undulator, as well as

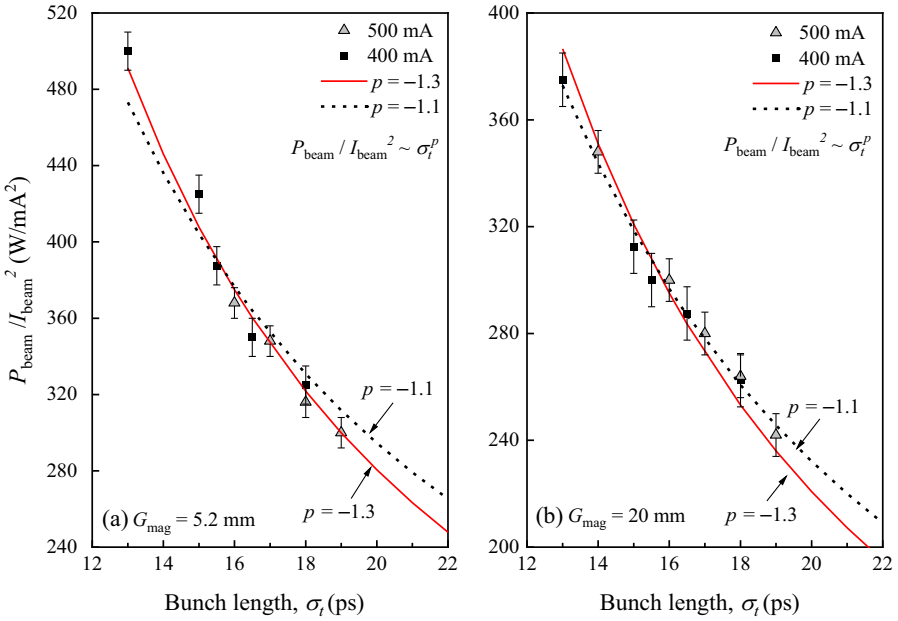

FIG. 14. Dependence of beam-induced heat-load on bunch length, (a) $G_{mag} = 5.2$ mm and (b) $G_{mag} = 20$ mm. The measurement conducted at $T_{mag} = 80$ K.

the relative magnetic field errors due to the thermal effects, are approximated as follows:

$$B = B_0 \exp\left(b_1\left(\frac{G_{mag}}{\lambda_u}\right) + b_2\left(\frac{G_{mag}}{\lambda_u}\right)^2\right), \tag{8}$$

$$\frac{\Delta B}{B} = f\,\frac{(\Delta G_{mag})_{max}}{\lambda_u} + \left(\frac{\Delta B}{B}\right)_{B_r}, \tag{9}$$

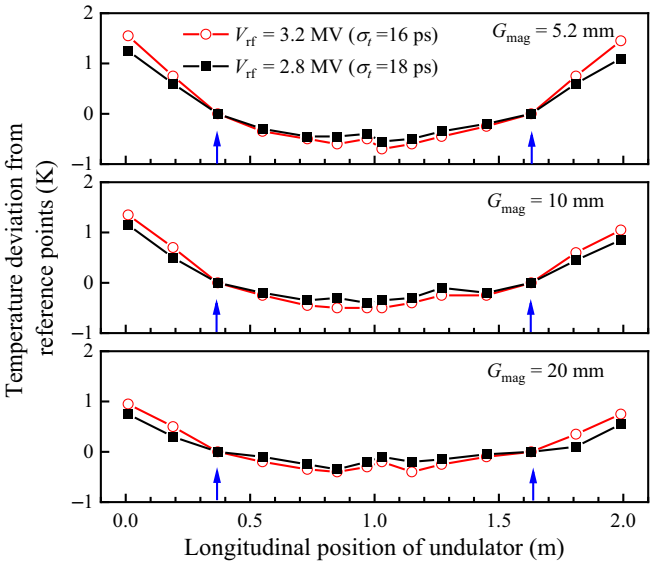

FIG. 15. Temperature deviation from reference points across magnet arrays at gaps of 5.2, 10, and 20 mm, with a beam current of 500 mA. The two arrows on each horizontal axis indicate reference points.

where $b_1 = -5.251$ and $b_2 = 2.079$ are fitting coefficients of magnetic field, $f = b_1 + 2b_2(G_{mag}/\lambda_u)$. The first term in Eq. (9) is derived from the thermal expansion, and the second term is from the temperature dependence of the permanent magnet's remanence.

The change of magnet gap per unit temperature at $T_{mag} = 80$ K has been measured as -2.5 μm/K. Based on this measurement, the first term of Eq. (9) is estimated to be 1.4×10^{-3} when the magnet gap is 5.2 mm and the f value is -3.86. Figure 10 shows that the temperature coefficient of the magnetic field effect is -0.06%/K at 80 K. As a result, the second term of Eq. (9) is -1.3×10^{-3}, leading to a net relative field error of 9.6×10^{-5}. At a gap of 5.2 mm with $K = 1.42$, this field error leads to a maximum rms phase error of less than 0.2°. So, the additional phase errors resulting from beam-induced heating shall not significantly affect the spectral performance.

4. Effect of undulator gap on the beam-induced heating

The beam-induced heat load at different magnet gaps was measured at a beam current of 500 mA, as shown in Fig. 16. It can be seen that the beam-induced heat load increases as the gap is decreased. The maximum beam-induced heating power recorded was 112 W at a 4.8 mm gap with a bunch length of 16 ps. However, if the gap decreases below 4.8 mm, beam-induced heat load can exceed the cooling margin, leading to an uncontrolled temperature gradient in the magnet arrays. On the other hand, by increasing the bunch length from 16 to 18 ps, there was an approximate reduction of 20 W across all gaps. So, a longer bunch length plays a crucial role in maintaining low

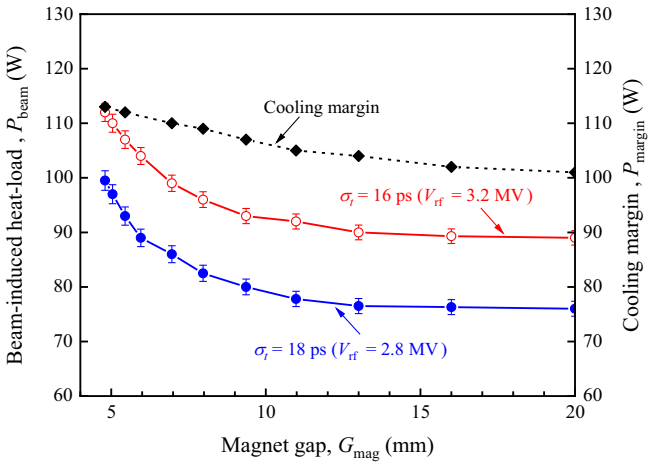

FIG. 16. Magnet gap dependence of beam-induced heat load, P_{beam}, measured at 500 mA with rf voltages 2.8 and 3.2 MV.

beam-induced heating in a CPMU. From the perspective of beam-induced heating, the current design of CU15, using conduction cooling with two cryocoolers, is thought to be feasible to operate at a gap of 4 mm or less in most of the fourth-generation storage rings, provided the bunch length is sufficiently long.

5. Comparison between calculated and measured beam-induced heat load

The beam-induced heat load measured at 500 mA with a magnet gap of 20 mm is about one order of magnitude higher than the calculated value (compare Figs. 12 and 16). The discrepancies between the measured and calculated heat loads persist at approximately constant values of 80 and 65 W for bunch lengths of 16 and 18 ps, respectively. These discrepancies are independent of gaps but vary with bunch length. These results suggest that the main factor contributing to this inconsistency may be the external microwave power derived from beam power loss due to the geometric impedance of various components outside CU15. Examples include the BPM, bellows, and other vacuum components located upstream or downstream of CU15. It is possible to calculate the beam energy loss attributable to each component of the storage ring. However, some of the energy loss is either trapped near the components or becomes microwaves propagating along the orbit and entering the CU15. Consequently, quantitative estimation of the entry of microwaves and their interactions within CU15 poses a challenging task.

Nevertheless, it is important to emphasize that the beam-induced heat load resulting from geometric impedance increases quadratically with the beam current. Therefore, when a CPMU operates at high beam currents, it becomes imperative to carefully design the transition taper in order to minimize beam power loss (microwave production) due to the geometric impedance.

C. Vibration issue from cryocoolers

The use of cryocoolers raises concerns about vibrations, that may affect the stable operation of the storage ring. Consequently, it is important to employ cryocoolers with low-vibration type. Since the field integral in the undulator is almost zero, the vibration from the cold heads is not expected to cause significant field integral errors that would

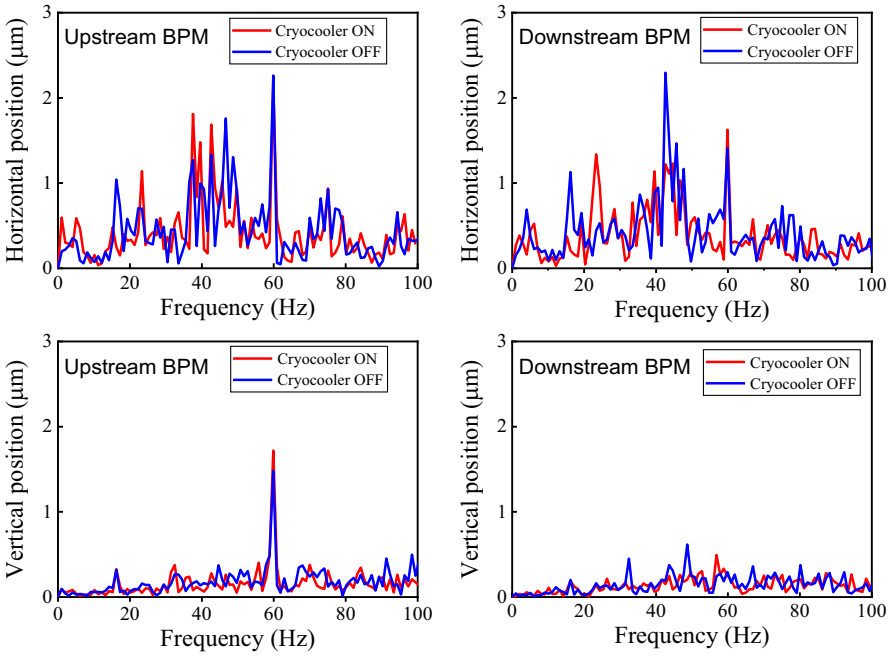

FIG. 17. Positions measurements from the two BPMs between the cryocooler switch on and off.

affect closed orbit distortion in the storage ring. However, if the vibrations are transmitted to the adjacent beam position monitors (BPMs), it may lead to faulty beam position feedback control. So, the vertical and horizontal positions measured from the two BPMs between the activation and deactivation of the cold heads are checked. These two BPMs are installed after bellows to isolate the vibration. Based on the results presented in Fig. 17, it is evident that the signals from the BPMs are not significantly influenced by vibrations from the cold heads. In practical terms, this level of vibration has a negligible impact on the beam control in the TPS storage ring.

V. CONCLUSION

The cryogenic permanent magnet undulator, CU15, with a period length of 15 mm and a period number of 133 has successfully operated in the TPS storage ring at NSRRC with a beam current of 500 mA for more than 3 years. In CU15, which uses PrFeB magnets, the temperature of magnets is kept at 80 K with a conduction cooling system based on cryocoolers. The effective magnetic field of 1.33 Tesla is obtained with a magnet gap of 4.2 mm and 1.02 Tesla with a magnet gap of 5.2 mm. This undulator has integrated several new technologies to ensure long-term stability in vacuum, cryogenic, and magnetic performance. The precise control of magnet temperatures guarantees consistent and reproducible photon energy spectra.

The development of CU15 placed significant emphasis on low phase error characteristics. To achieve this objective, various measures were employed, such as incorporating OFHC copper in-vacuum girders, optimizing the number of bellows-link rods, implementing a precise temperature control system, and integrating force-compensating spring modules into the mechanical frame. Through several iterations of field corrections, the rms phase error was successfully reduced to less than 2.6° at all gaps.

The beam-induced heating mechanism is attributed to broadband impedance, making it sensitive to changes in both beam current and bunch length. The primary heat load on magnet arrays is generated by the microwave power caused by beam energy loss due to geometric impedance. At a small gap, the resistive wall heating increases and becomes a significant factor in the beam-induced heating mechanism. At a beam current of 500 mA, the measured beam-induced heating power at CU15 is approximately 90 W at a gap of 20 mm with a bunch length of 16 ps. The measured heat load is much higher than the calculated beam power loss derived from the CU15 components (transition tapers and magnet arrays). The discrepancies seem to be linked to the external microwave power, which is determined by the beam power loss from the geometrical impedance of various components outside CU15.

In general, the conduction-cooled CPMU with cryocoolers is feasible for operation at a small gap in most fourth-generation storage rings, provided the bunch length is properly controlled.

ACKNOWLEDGMENTS

The author would like to thank Dr. Alex. Chao (SLAC) for valuable discussions on the impedance issue and Dr. Jia-Ye Chen (a former researcher at NSRRC) for the calculation of the longitudinal loss factor. This work was supported by National Science and Technology Council, Taiwan.

[1] E. Wallén and G. LeBlanc, Cryogenic system of the MAX-Wiggler, Cryogenics **44**, 879 (2004).

[2] C. Benabderrahmane *et al.*, Development and operation of a $Pr_2Fe_{14}B$ based cryogenic permanent magnet undulator for a high spatial resolution x-ray beam line, Phys. Rev. Accel. Beams **20**, 033201 (2017).

[3] C. Benabderrahmane, P. Brumund, J. Chavanne, D. Coulon, G. Le Bec, B. Ogier, and R. Versteegen, *Development and construction of cryogenic permanent magnet undulators for ESRF-EBS*, in Proceedings of 13th International Particle Accelerator Conference, IPAC-2022, Bangkok, Thailand (JACoW, Geneva, Switzerland, 2022).

[4] Y. He, M. Qian, H. Wang, W. Zhang, and Q. Zhou, *Cryogenic permanent magnet undulator of SSRF*, in *Proceedings of 9th International Particle Accelerator Conference, IPAC-2018 Vancouver, Canada* (JACoW, Geneva, Switzerland, 2018).

[5] J. C. Schouten and E. C. M. Rial, Electron beam heating and operation of the cryogenic undulator and superconducting wigglers at diamond, in *Proceedings of the 2nd International Particle Accelerator Conference, IPAC-2011, San Sebastián, Spain* (EPS-AG, Spain, 2011), THPC179.

[6] S. Casalbuoni, A. Grau, M. Hagelstein, R. Rossmanith, F. Zimmermann, B. Kostka, E. Mashkina, E. Steffens, A. Bernhard, D. Wollmann, and T. Baumbach, Beam heat load and pressure rise in a cold vacuum chamber, Phys. Rev. ST Accel. Beams **10**, 093202 (2007).

[7] Y. Ivanyushenkov *et al.*, Development and operating experience of a short-period superconducting undulator at the Advanced Photon Source, Phys. Rev. ST Accel. Beams **18**, 040703 (2015).

[8] R. Voutta, S. Gerstl, S. Casalbuoni *et al.*, Cold vacuum chamber for diagnostics: Analysis of the measurements at the Diamond Light Source and impedance bench measurements, Phys. Rev. Accel. Beams **19**, 053201 (2016).

[9] J. C. Huang, H. Kitamura, C. S. Yang, C. K. Yang, and C. W. Chen, Operational experiences of two CPMUs at Taiwan Photon Source, in *Proceedings of 14th International Particle Accelerator Conference, IPAC-2023, Venice, Italy* (JACoW, Geneva, Switzerland, 2023), WEPM104.

[10] J. C. Huang, H. Kitamura, C. K. Yang, C. H. Chang, C. H. Chang, and C. S. Hwang, Challenges of in-vacuum and cryogenic permanent magnet undulator technologies, Phys. Rev. Accel. Beams **20**, 064801 (2017).

[11] C. K. Yang, J. C. Huang, C. S. Yang, C. W. Chen, Y. L. Chu, and C. S. Hwang, Field measurement of a cryogenic permanent magnet undulator at TPS, IEEE Trans. Appl. Supercond. **30**, 4100205 (2019).

[12] C. W. Chen, Y. Y. Hsu, Y. L. Chu, H. Chen, C. K. Yang, and J. C. Huang, A temperature-dependent calibration of Hall probes for CPMU, IEEE Trans. Appl. Supercond. **32**, 9001805 (2022).

[13] D. Hidas, T. Shaftan, and T. Tanabe, Emittance and energy spread compensation for current and future low emittance synchrotron light sources, Phys. Rev. Accel. Beams **24**, 081601 (2021).

[14] J. C. Huang, H. Kitamura, C. S. Yang, T. Kohda, S. Mizumoto, C. Y. Yang, C. H. Chang, and C. S. Hwang, Force-compensating spring modules of self-contained type for small phase error performance in in-vacuum undulators, Nucl. Instrum. Methods Phys. Res., Sect. A **1013**, 165650 (2021).

[15] K. J. Kim, Angular distribution of undulator power for an arbitrary deflection parameter K, Nucl. Instrum. Methods Phys. Res., Sect. A **246**, 67 (1986).

[16] B. Podobedov, Resistive wall wakefields in the extreme anomalous skin effect regime, Phys. Rev. ST Accel. Beams **12**, 044401 (2009).

[17] W. Bruns, http://www.gdfidl.de.